# Towards ultrasound travel time tomography for quantifying human limb geometry and material properties

Jonathan R. Fincke[1], Micha Feigin[2], Germán A. Prieto[3], Xiang Zhang[1], Brian Anthony[1]

[1]Department of Mechanical Engineering, Massachusetts Institute of Technology, Cambridge, MA, 02139 USA;
[2]Department of Media Arts and Sciences, Massachusetts Institute of Technology, Cambridge, MA, 02139 USA;
[3]Department of Earth Atmospheric and Planetary Sciences, Massachusetts Institute of Technology, Cambridge, MA, 02139 USA

## ABSTRACT

Sound speed inversions made using simulated time of flight data from a numerical limb-mimicking phantom comprised of soft tissue and a bone inclusion demonstrate that wave front tracking forward modeling combined with $L_1$ regularization could lead to accurate estimates of bone sound-speed. Ultrasonic tomographic imaging of limbs has the potential to impact prosthetic socket fitting, as well as detect and track muscular dystrophy diseases, osteoporosis and bone fractures at low cost and without radiation exposure. Research in ultrasound tomography of bones has increased in the last 10 years, however, methods delivering clinically useful sound-speed inversions are lacking. Inversions for the sound-speed of the numerical phantoms using $L_1$and $L_2$ regularizations are compared using wave front forward models. The simulations are based on a custom-made cylindrically-scanning tomographic medical ultrasound system (0.5 – 5 MHz) consisting of two acoustic transducers capable of collecting pulse echo and travel time measurements over the entire 360° aperture.

**Keywords:** Ultrasound tomography, bone, migration, reverse time migration

## 1. INTRODUCTION

The majority of existing ultrasound imaging algorithms and systems are designed for applications involving soft tissues such as imaging for pre-natal health, cardiac imaging, detection of breast cancer and therapeutic uses. Clinical ultrasound systems for 3-D imaging and quantification of hard tissues such as bone *in vivo* are currently non-existent. Applications for an ultrasound system capable of imaging and quantifying bone properties range from improving prosthetic fitting to osteoporosis monitoring and detection to bone fracture detection. Recently, the authors developed a cylindrically scanning ultrasound tomography system for the purposes of creating clinically useful pulse-echo and sound-speed inversion images of bone and surrounding soft tissue.[1] This paper describes initial work on the algorithm development using data from wave equation simulations that broadly mimic the geometry, transducer positioning capabilities of the scanner as well as the signal to noise ratio (SNR) of the data acquisition electronics.

The majority of ultrasound tomography research over the last twenty years has focused on the detection of breast cancer.[2–6] A number of studies have shown the promise of ultrasound tomography methods for imaging and quantifying bone properties, however, these studies have not lead to clinical testing of a system for imaging and quantifying bone and surrounding soft tissue properties.[7–9] There is also a significant body of literature using ultrasound to derive the material properties of bone using single or a handful of transmit receive pairs.[10–12] These studies have focused on using single parameters like travel time, frequency dependent attenuation and backscatter coefficients to deduce the properties of the bone under test, rather than generating images of some or all of these properties.

Generating clinically useful pulse-echo and sound-speed inversion images of regions of the body where bones are present leads to significant algorithmic and measurement challenges. These challenges are primarily exist because

Medical Imaging 2016: Ultrasonic Imaging and Tomography, edited by Neb Duric, Brecht Heyde, Proc. of SPIE
Vol. 9790, 97901S · © 2016 SPIE · CCC code: 1605-7422/16/$18 · doi: 10.1117/12.2218387

human bones have sound-speed and density values that are approximately double that of the surrounding tissue and attenuation that can be an order of magnitude greater than soft tissue. Furthermore, the ability of bone to support shear waves has the potential to introduce artifacts into pulse-echo images of bone if not properly accounted for. The large changes in sound-speed and density leads to strong reflections that can shadow other anatomical regions of interest in pulse echo imaging as well as significantly alter the arrival of reflected signals due to the difference in sound-speed between bone and soft tissue. In terms of travel time measurements and inversions, the presence of bone significantly degrades the SNR of the first arrival due to strong attenuation in the bone and reflections at the bone interfaces. The large sound-speed changes at the bone interface also create strong refractions which must be taken into account. The shear waves generated in bone can result in multiple arrivals in the pulse-echo data that are not be accounted for in conventional soft tissue pulse-echo imaging algorithms.

Studies using ultrasound to image and quantify bone have relied on inversion schemes that often left out in some capacity, refraction, shear waves a priori information, or a test object surrounded by soft tissue.[7–9,13] Much of the propagation physics were originally left out from inversions due to the lack of computational power available at the time of these studies. The most recent studies suggest improvements in ultrasound imaging and quantification of bone material properties can be made through improved modeling of the propagation physics and constraining inversions with a priori information.[8]

In this numerical study a simple numerical phantom of a bone surrounded by fat and muscle is used to generate a synthetic data set, although shear waves are not simulated. The simulated data set is used to explore the potential for travel time ultrasound tomography techniques to invert for bone and surrounding soft tissue sound-speed. Three travel time tomography inversion schemes are implemented, one with $L_1$ regularization, one with $L_2$ regularization and a third which inverts for whole sections of the domain rather than individual pixels. All three inversion schemes include a priori information from pulse echo images.

## 2. METHODS

The synthetic data set generated for this paper is based on a custom-made dual-transducer cylindrically-scanning immersion ultrasonic tomographic scanner (Fig. 1). Both transducers can independently travel over the entire 360° aperture and translate ~7cm vertically allowing for multiple 2-D slice images of a target to be captured. The two transducer setup also enables rapid development of scanning procedures and testing of transducers with varying beam properties and frequency. Further details describing the system can be found in Zhang *et al*[1].

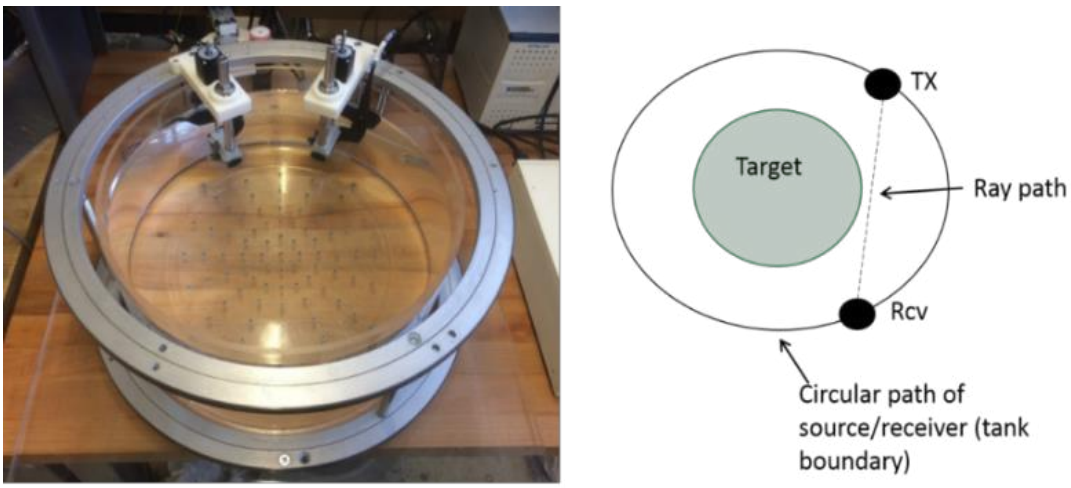


Figure 1: Image and schematic of the tomographic ultrasound system. The system is comprised of two transducers that can move independently both around the tank and up and down.

The synthetic data set is processed as if it were acquired with the physical system. The processing pipeline from raw data to a sound-speed map can be separated into four steps that will be covered in more detail below.

1. Creation of data set via acoustic wave equation simulations.
2. Picking of travel times from the simulated data set.
3. Construction of pulse-echo images and segmentation of the images to generate an initial guess for the sound-speed map.
4. Estimation of the sound-speed map using a ray based travel time inversion for sound-speed.

### 2.1 Simulation

The K-wave ultrasound simulation package is used to generate the synthetic data set using a simple 2-D numerical phantom of a human long bone (Fig. 2) that loosely resembles a femur.[14] The simulations include velocity and density variations as well as attenuation. Elastic waves within the bone region are not simulated. The simulation domain is 0.2165 m x 0.2165 m using a 512 x 512 grid. The source is a point source that is appropriately spatially smoothed to avoid aliasing with a central frequency of 1.0 MHz and 1.0 MHz bandwidth. The receivers are defined as point receivers. In practice the scanner system employs a cylindrically focused source and the receivers have ~90° beam width. The sound-speed, density and attenuation values used for fat water muscle, bone and marrow are taken from the literature[15,16] and are shown in table 1. It should be noted the attenuation value of human skull bone is used for the bone region since it is an upper bound on bone attenuation.

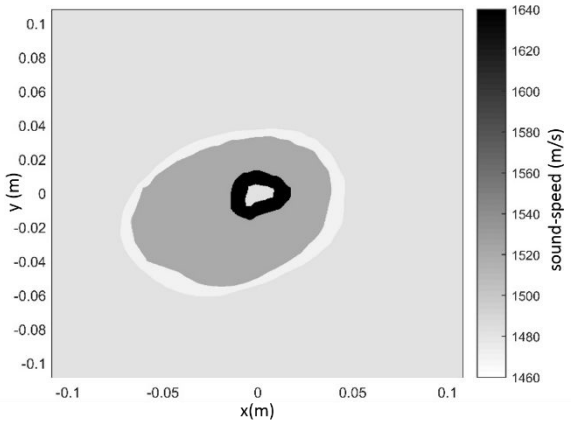


Figure 2: Sound-speed map for the simple numerical phantom of a human long bone used for the simulations. The ambient medium is water (gray) and the phantom has fat (light gray), muscle (dark gray), bone (black) and marrow (light gray inside bone).

Table 1. Material properties assigned to simulated medium. All values taken from[15,16] except for marrow which was given the same properties as water.

| Tissue type | Sound-speed $\frac{m}{s}$ | Density $\frac{kg}{m^3}$ | Attenuation $\frac{dB}{m}$ at 1.0 MHz |
|---|---|---|---|
| Water | 1480 | 1000 | 0.22 |
| Fat | 1470 | 986 | 50 |
| Muscle | 1520 | 1052 | 95 |
| Bone | 3460 | 1800 | 1500 |
| Marrow | 1480 | 1000 | 0.22 |

Three scan types are used to generate the synthetic data set, a tomographic scan, a pulse echo scan and a synthetic aperture pulse-echo scan. For this paper a single tomographic scan, Fig. 3a, consists of 360 transmissions (k-wave simulations) to 300 receiver positions with 1.2° sepperation located on the opposite side of the tank from the transmitter. A pulse echo scan, Fig. 3b, consists of 1533 transmissions (k-wave simulations) separated by 0.235°. A point receiver is also placed at the source position such that pulse echo data is captured for each transmission. A

synthetic aperture scan, Fig. 3c, consists of 8 transmissions separated by 45° increments with 300 receivers to either side of the transmitter.

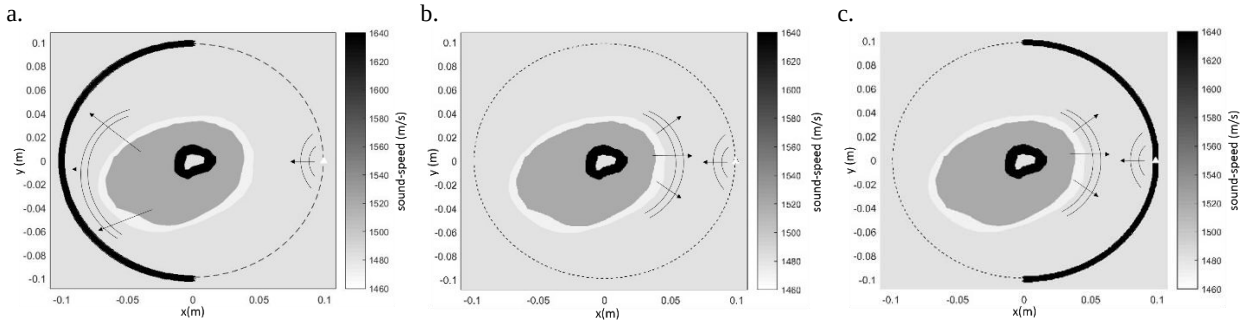


Figure 3: Scan patterns to acquire data for travel time, migration and RTM algorithms. The black dots are receivers and the white triangles are transmitters. a.) Scan pattern for the travel time data acquisition. The transmitter and receivers move along the dashed line and an acquisition is taken at 1° increments. b.) Migration scan pattern. The transmitter and receiver travel along the dashed line together transmitting at 0.235° increments along the 360° aperture. c.) RTM scan pattern. The receivers and source travel along the dashed line and an acquisition is taken at 45° degree increments.

### 2.2 Travel time picking

The travel times are picked using the Akaike Information Criterion (AIC) and a matched filter to find the peak of the first arrival. The AIC is a quantitative criterion for picking a model that describes a process that will minimize the information loss by choosing a particular model for the process.[17] The AIC was originally adapted for travel time picking in seismology, however, some researchers have successfully applied the method to ultrasound tomography.[17]

The AIC value is calculated using equations 1 and 2 from Li *et al*[17]. The minimum in the AIC value indicates the arrival of a signal.[17] Once the arrival of the signal is estimated a $2.0 * F\ \mu s$ window for the matched filter is defined starting at the first arrival point, where $F$ is an empirical SNR dependent multiplicative factor. The value of $F$ is typically ~2 for arrivals that travel through soft tissue or water and ~1 for arrivals that travel through bone.

A half period 500 kHz sine wave multiplied by a Hanning window is convolved with the window of data to remove noise and find the peak of the first arrival. The frequency of the matched filter is chosen to match the expected frequency content of the first arrival. The first arrival through bone is expected to predominantly contain the lowest transmitted frequency due to dispersion and smaller impact of attenuation at lower frequencies. It has been shown that the low frequency data arrives first in laboratory experiments.[8] Since the picks are done on simulated data, random noise is added to all the signals such that the SNR is equivalent to the SNR measured during initial testing of the physical scanner system.

### 2.3 Pulse-echo image reconstruction

Pulse echo images are generated using a migration algorithm on the pulse echo data.[18] The migration routine assumes that all scatterers in the medium are point scatterers, the medium has a constant sound-speed (1480 m/s for this paper), and that scatterers do not shadow each other. In practice, none of the assumptions will hold true and are not true for the numerical phantom presented here, particularly because of the bone inclusion. The migration algorithm is used, however, because the stated assumptions are similar to those made in conventional ultrasound systems which have successfully imaged the interior of the human body for decades. Therefore, it is expected the migration algorithm will capture the geometry of soft tissue areas and the outer geometry of the bone surface with sufficient accuracy.

The pulse echo images from the migration are segmented by hand to define sound-speed boundaries within the domain which in-turn define regions. These regions are assumed to be associated with either water, fat, muscle or

bone. Values for sound-speeds published in the literature[15,16] are assigned to the regions defined by the segmentation to create an initial guess for the sound-speed map.

The initial guess sound-speed map is first used in a reverse time migration[19,20] (RTM) to find the inner boundary of the bone. In order to run the RTM the synthetic aperture pulse-echo scan data is used. The RTM method is used to find the inner boundary of the bone because the RTM includes variations in sound-speed, reflections and refractions that characterize ultrasonic propagation through bone to create an image. Therefor it is expected the RTM method will provide the superior results compared to a migration based method. The forward solves needed to run the RTM are carried out using k-wave. Once the RTM image is generated it is segmented for the bone inner boundary and the bone region of the initial guess sound-speed map is updated based on this segmentation.

**2.4 Ray based travel time inversion for sound-speed**

The inversion for sound-speed values is done by solving the equation

$$d = Gm \tag{1}$$

for $m$ where $d$ is the travel time data generated by the travel time picker, $G$ is a matrix describing the path of the received signal through the domain and $m$ is the slowness (1/sound-speed) distribution within the domain. Rays connecting each receiver to each source must be calculated to create $G$. The rays are calculated by solving the eikonal equation via a wave front tracking program[21,22] and wavefronts are converted to rays after each simulation by following the normal to the first arrival wavefront from each receiver back to the source.

The system in (1) is generally over determined, unstable with a non-unique solution. Resolving this requires the addition of a regularization term to find a solution. Equation (1) is thus replaced with the following cost function, which is minimized with respect to $m$ using the gradient descent method.

$$C(m) = \|Gm - d\|_2^2 + \delta \|\nabla m\|_1 \tag{2}$$

The $L_2$ norm is utilized for the first term (the fidelity term) and a $L_1$ norm is used over the gradient term. The $L_1$ norm over the gradient term implies an assumption that the underlying sound-speed map is piecewise constant which allows for large discontinuities in the inverted sound-speed map. The more classic Tikhonov ($L_2$) regularization implies an assumption that the sound-speed map is smooth. This conflicts with the large gradient at the soft tissue -bone interface producing large errors in the bone sound speed reconstruction, as can be seen in the experimental results. In practice, a more robust version of the $L_1$ norm as described by Bar *et al*[23] is used to find a solution to equation (2).

A second related method of inversion is also developed where entire regions or blocks of the domain are inverted for as a single parameters in the inversion model. The pulse-echo segmentations described above define the regions. Such a block wise inversion can be thought of as a "perfect" $L_1$ regularization because the formulation forces the solution be made up of many piece-wise constant regions. The inversion is done by condensing the $G$ matrix into a matrix called $G_{block}$ defined as

$$G_{block_{i,b}} = \sum_{n=1}^{N_b} G'_{i,n,b} \ , \ i = 1 \dots N_{ttm} \ , \ b = 1 \dots N_{blocks} \tag{3}$$

$$G'_{i,j,b} = G_{i,j} \in B_b \ , \quad b = 1 \dots N_{blocks} \tag{4}$$

where $N_b$ is the number of pixels within the $b^{th}$ block in the domain, $N_{ttm}$ is the number of travel time measurements, $N_{blocks}$ is the number of blocks the domain is split into and $G'$ is a 3-D matrix that in each third dimension contains only the parts of $G$ that describe travel paths through the $b^{th}$ block of the domain. In practice $G'$ does not need to

be calculated but is included here to formally describe $G_{block}$. The cost function $C_b(m)$ for the block-wise inversion is given by

$$C_b(m) = \|G_{block}m - d\|_2^2 \tag{8}$$

and is minimized via a gradient descent algorithm.

The inversion scheme is iterative for all three methods and is started using the initial sound-speed map generated from the pulse echo data. During each iteration the eikonal equation is solved and $C(m)$ is minimized, the resulting $m$ from the previous iteration is then fed into the next one. The inversion is run until the residual between the model and the data (the travel times) no longer changes. Since the inversion is being done on simulated data, Gaussian noise with +/- 7.5 $\mu m$ standard deviation and zero mean is added to the source and receiver positions to account for their position uncertainties in laboratory measurements.

## 3. RESULTS

### 3.1 Pulse-echo imaging and segmentation

The image in Fig. 4a generated from the migration routine captures the fat-water, fat-muscle, muscle-bone and bone-marrow interfaces as expected. There are some artifacts in the muscle region that are most likely due to the bone. The dark ring in the image is due to an artifact in the simulation data that occurs for a short time at the bi-static source/receiver position. Since the artifact does not affect the image of the phantom it was not removed. The segmentation is plotted over the true numerical phantom in Fig. 4b. The inner boundary of the bone is not accurately located; this is expected due to the large sound-speed difference between bone and soft tissue. An initial guess of the sound-speed map is created from this segmentation using reported sound-speed values from the literature and fed into the RTM algorithm.

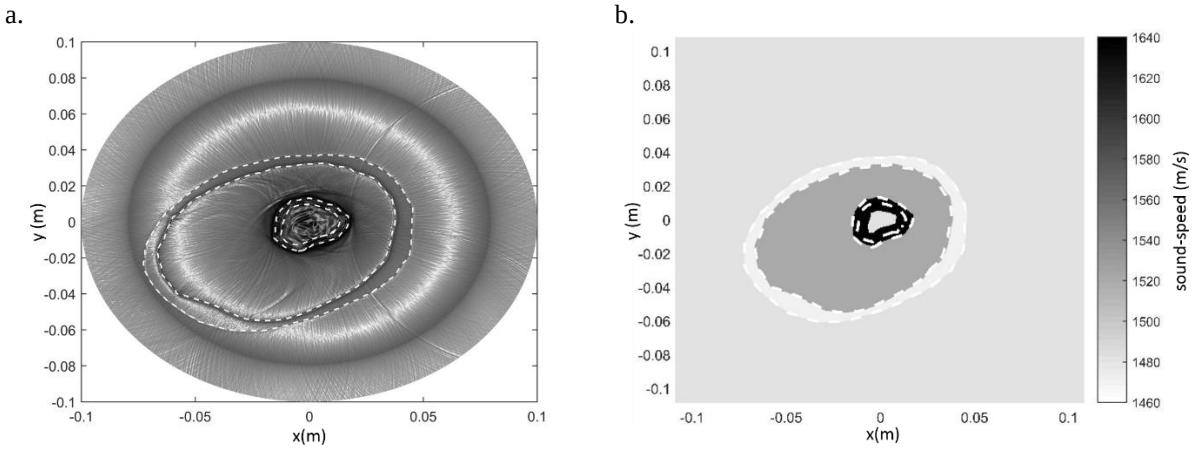


Figure 4: Resulting image from the migration algorithm and segmented boundaries. a.) Image generated by the migration algorithm. The soft tissue boundaries and outer bone boundary are captured clearly but the inner boundary of the bone is harder to make out. The white dashed lines are the segmentation of the image. b.) segmentation overlaid on the sound-speed map of the numerical phantom. The soft tissue boundaries and the bone muscle boundary are accurately captured. The inner boundary of the bone is not correctly located.

The RTM algorithm is run twice such that bone inner boundary location estimate is iteratively improved. The inner boundary of the bone is segmented from the first RTM image and used to update the initial velocity model. The RTM is run a second time on the updated velocity model and the resulting image (Fig. 5a) is segmented. The final segmented contours of the phantom are plotted in Fig. 5b showing a better estimation of the bone inner boundary compared to Fig. 4b.

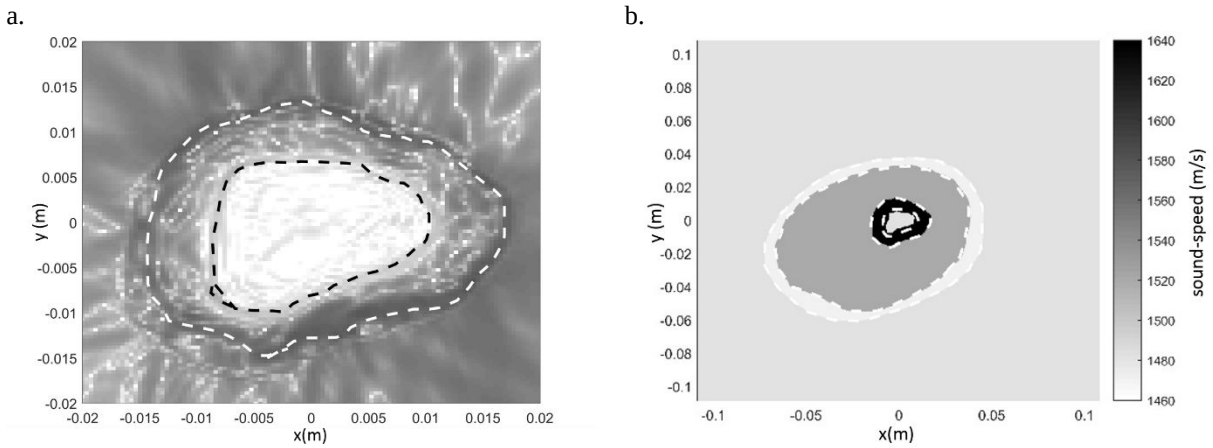


Figure 5: Close up of the bone from the RTM image and the final segmentation of the pulse echo images. a.) The bone region from the RTM image. The inner bone boundary is the marked by the black dashed line and the outer bone boundary is marked by the dashed white line. b.) The final segmentation plotted on top of the true sound-speed map of the numerical phantom.

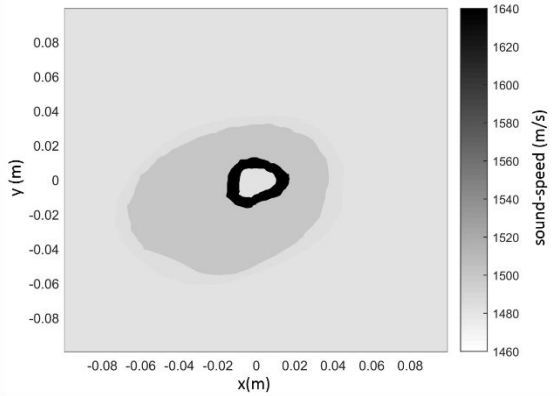


Table 2: Sound-speed values for the initial guess sound-speed map.

| Tissue type | Sound-speed $\frac{m}{s}$ |
|---|---|
| Water | 1480 |
| Fat | 1485 |
| Muscle | 1500 |
| Bone | 3200 |
| Marrow | 1480 |

Figure 6: Initial guess sound-speed map for the travel time inversion. Overall the geometry of the initial guess is close the phantom geometry except for the inner boundary of the bone. The skin-water boundary is difficult to pick out but is present.

### 3.3 Sound-speed inversion

The sound-speed inversions show that sound-speed of the bone and soft tissue can be estimated from the synthetic data set using travel time tomography techniques. Inversions (Fig. 7) are done using $L_1$ and $L_2$ regularization as well as the block method. In the bone region the $L_1$ based inversion shows a broad region of high sound-speed (Fig. 7b) compared to the $L_2$ inversion (Fig.7d). The $L_1$ regularization also has a smaller error in the mean sound speed of the bone region (table 3). Both regularizations estimate the water, fat and muscle sound-speeds with similar spatial resolution and error (tables 3 and 4). The estimates for marrow are not included because the direct arrival rays do not sample the marrow region of the domain.

The block based inversion (Fig. 7e) has a spatial resolution equivalent to the pulse echo image (since the block regions are defined by the pulse-echo image) and errors in velocity for water, fat and muscle that are nearly equivalent to the $L_1$ and $L_2$ regularized inversions (table 5). In the bone region, the block based method has the smallest error among all the methods (table 5). In Fig. 7f a slice through one wall of the bone is shown for all three inversion methods; it can be seen that the $L_1$ regularization significantly improves the resolution of the inversion compared to the $L_2$ regularization.

Both the $L_1$ and $L_2$ based regularizations have significant artificial spatial variation in sound-speed values within the bone whereas the block based approach provides a single estimate of the bone sound-speed (Fig. 7f). All

of the inversion methods result in bone regions that are narrower than the ground truth (Fig. 7f) which is likely due to the fact that the bone thickness is underestimated in the initial guess sound-speed map due to the difficulty in accurately locating the inner boundary of the bone.

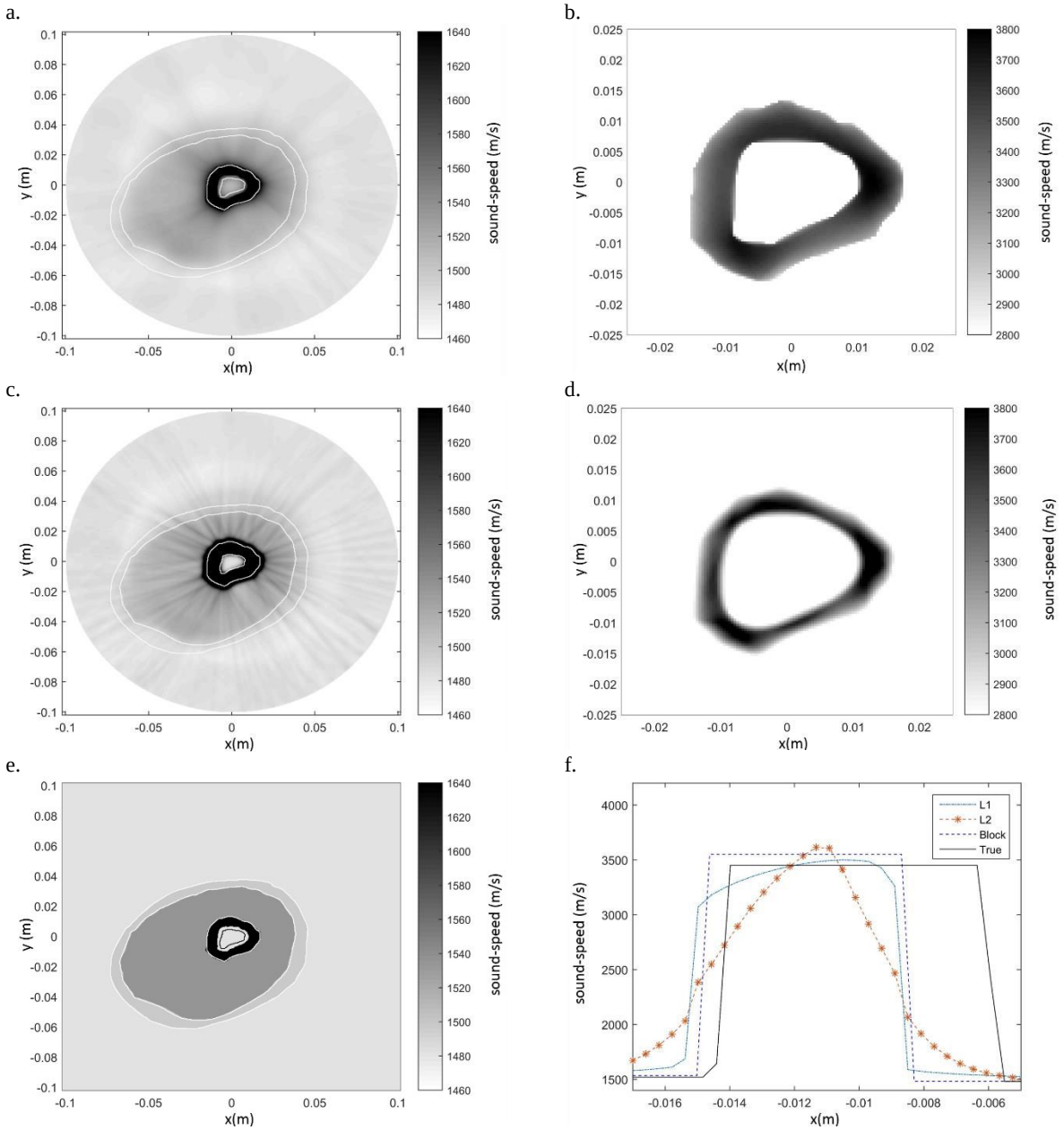


Figure 7: Sound-speed inversions using $L_1$ and $L_2$ regularization as well a block based approach. The white lines in a,c and e are the tissue boundaries of the numerical phantom. a.) The $L_1$ regularized inversion. The bone-muscle boundary is well preserved and artifacts are minimal. b.) Zoom-in of the bone region. Note the strong contrast between the background and the bone. c.) The $L_2$ regularized inversion. The size of the bone is larger than the $L_1$ inversion and more artifacts are present. d.) Zoom-in of the bone region. Note the how the bone region appears much thinner than the $L_1$ regularized inversion. e.) The block based inversion. The black contour is the true location of bone inner boundary. The resolution is much higher compared to the $L_1$ and $L_2$ regularized inversions due to the dependence of the inversion on the pulse-echo data. f.) Cross-section of a single wall of the bone with all three inversions and the ground truth plotted. None of the inversion accurately estimate the bone thickness but the $L_1$ and block based inversions provide the best estimates of the bone sound-speed.

Table 3: Summary of $L_1$ regularized inversion results. Marrow results not shown because the first arrival rays do not pass through the marrow region.

| Tissue type | Mean sound-speed $\frac{m}{s}$ | Error $\frac{m}{s}$ | % Error |
|---|---|---|---|
| Water | 1482 | 3 | 0.1 |
| Fat | 1497 | 29 | 1.9 |
| Muscle | 1526 | 8 | 0.4 |
| Bone | 3394 | 116 | -1.9 |
| Marrow | - | - | - |

Table 4: Summary of $L_2$ regularized inversion results. Marrow results not shown because the first arrival rays do not pass through the marrow region.

| Tissue type | Mean sound-speed $\frac{m}{s}$ | Error $\frac{m}{s}$ | % Error |
|---|---|---|---|
| Water | 1483 | 3 | 0.1 |
| Fat | 1469 | 26 | 1.8 |
| Muscle | 1532 | 12 | 0.8 |
| Bone | 3090 | 370 | -10.7 |
| Marrow | - | - | - |

Table 5: Summary of block wise inversion results Marrow results not shown because the first arrival rays do not pass through the marrow region.

| Tissue type | Sound-speed $\frac{m}{s}$ | Error $\frac{m}{s}$ | % Error |
|---|---|---|---|
| Water | 1481 | 1 | 0.1 |
| Fat | 1497 | 27 | 1.8 |
| Muscle | 1535 | 15 | 1.0 |
| Bone | 3551 | 91 | 2.6 |
| Marrow | - | - | - |

There are significant streaky artifacts emanating from the bone region in both the $L_1$ and $L_2$ regularized inversions that are not present in the block based inversion. The artifacts are almost certainly due to the way the rays "sample" the domain. Due to the high sound-speed of the bone, most of the direct arrivals travel through the bone region. As a result, a much larger number of rays pass through the bone region of the domain compared to the water or soft tissue areas (Fig. 8). It can also be seen that the artifacts in the $L_1$ and $L_2$ regularized inversions have the same structure as the sampling pattern in Fig. 8.

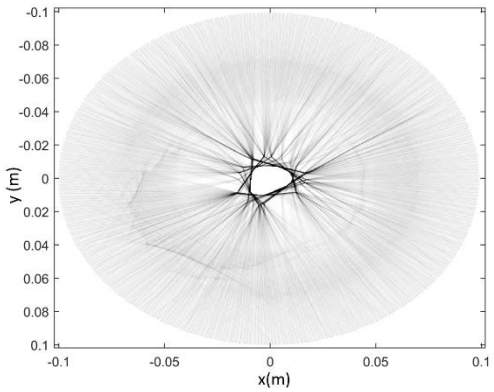


Figure 8: Sampling of the domain by the first arrival rays. The darker colors indicate more rays traveled through a particular region. Clearly the bone region has more rays passing through it than any other region of the domain. This sampling pattern is most likely causing the artifacts in the $L_1$ and $L_2$ regularized inversions.

## 4. CONCLUSIONS

A synthetic data set collected on a simple numerical phantom of a human long bone is used to demonstrate the potential of imaging and quantifying bone and surrounding soft tissue geometry and material properties using ultrasound tomographic techniques. The synthetic data set mimics the performance of a recently constructed ultrasound scanner built by the authors and contains pulse-echo and one-way time of flight measurements.[1] Segmentations of the pulse echo images constructed from the synthetic data are used to create an a priori initial guess for the sound-speed inversions. Three inversion methods were tested, one with $L_1$ regularization, one with $L_2$ regularization and third method that inverts for the sound-speed of entire regions or blocks of the domain.

The $L_1$ and block based inversions perform the best based on their superior accuracy and resolution compared to the $L_2$ regularized inversion. The $L_2$ regularized inversion over-smooth's the sound-speed map leading to large errors in the bone velocity estimates and geometry. Both the $L_1$ and $L_2$ based regularized inversions contain artifacts most likely due to the density of rays that pass through the bone region. The block based inversion does not contain these artifacts while simultaneously providing accurate, high-resolution results.

The inclusion of an initial guess sound-speed map enabled reasonable estimates of tissue sound-speed to be made in the presence of bone but can also bias the results. As seen in Fig.7a,c,e and f the inner boundary of the bone is not accurately located. Further work on obtaining an improved first estimate of the bone inner boundary may significantly improve the results, especially for the block wise inversion.

The block inversion may not be suitable for many applications such as detection of breast cancer because it relies so heavily on the pulse-echo imagining. The danger in using an inversion method that relies on the segmentations from the pulse echo images is that certain structures could be missed or severely distorted leading to large errors in sound-speed estimates. It is unclear at this point if the block based methods will perform well when applied to data from a human subject or even a more realistic numerical phantom. The main advantages of the block based method are the high resolution and accuracy of the method without having to resort to a full waveform inversion. These advantages make it worth testing further, however, it is possible that full waveform inversion approaches will be the most appropriate tomographic technique for imaging and quantifying bone with ultrasound.

## 5. ACKNOWLEDGEMENTS

This work was supported by the Department of Defense (DoD) through the National Defense Science & Engineering Graduate Fellowship (NDSEG) Program, The MIT Skoltech Initiative and the MIT Lincoln Laboratory.

## REFERENCES

[1] Zhang, X., Fincke, J., Kuzmin, A., Lempitsky, V.., Anthony, B., "A single element 3D ultrasound tomography system," Proc. Annu. Int. Conf. IEEE Eng. Med. Biol. Soc. EMBS **2015-Novem**, 5541–5544 (2015).

[2] Li, C., Duric, N., Littrup, P.., Huang, L., "In vivo breast sound-speed imaging with ultrasound tomography," Ultrasound Med. Biol. **141**(4), 520–529 (2008).

[3] Ruiter, N. V., Zapf, M., Hopp, T.., Gemmeke, H., "Experimental evaluation of noise generated by grating lobes for a sparse 3D ultrasound computer tomography system," Proc SPIE **8675**, 86750N – 86750N – 8 (2013).

[4] Rouyer, J., Mensah, S., Franceschini, E., Lasaygues, P.., Lefebvre, J. P., "Conformal ultrasound imaging system for anatomical breast inspection," IEEE Trans. Ultrason. Ferroelectr. Freq. Control **59**(7), 1457–1469 (2012).

[5] Hooi, F. M.., Carson, P. L., "First-arrival traveltime sound speed inversion with a priori information," Med. Phys. **41**(8), 082902 (2014).

[6] André, M., Wiskin, J.., Borup, D., "Clinical Results with Ultrasound Computed Tomography of the Breast," [Quantitative Ultrasound in Soft Tissues], 315–341 (2013).

[7] Carson, P. L., Oughton, T. V., Hendee, W. R.., Ahuja, a S., "Imaging soft tissue through bone with ultrasound transmission tomography by reconstruction.," Med. Phys. **4**(4), 302–309 (2015).
[8] Lasaygues, P., Ouedraogo, E., Lefebvre, J.-P., Gindre, M., Talmant, M.., Laugier, P., "Progress towards in vitro quantitative imaging of human femur using compound quantitative ultrasonic tomography.," Phys. Med. Biol. **50**(11), 2633–2649 (2005).
[9] Sehgal, C. M., Lewallen, D. G., Nicholoson, J. A., Robb, R. A.., Greenleaf, J. F., "Ultrasound transmission and reflection computerized tomography for imaging bones and adjoining soft tissues," IEEE Ultrason. Symp., 849–852 (1988).
[10] Cardoso, L., Teboul, F., Sedel, L., Oddou, C.., Meunier, A., "In Vitro Acoustic Waves Propagation in Human and Bovine Cancellous Bone," J. Bone Miner. Res. **18**(10), 1803–1812 (2003).
[11] Padilla, F., Akrout, L., Kolta, S., Latremouille, C., Roux, C.., Laugier, P., "In Vitro ultrasound measurement at the human femur," Calcif. Tissue Int. **75**(5), 421–430 (2004).
[12] Wear, K. A., "Ultrasonic scattering from cancellous bone: A review," IEEE Trans. Ultrason. Ferroelectr. Freq. Control **55**(7), 1432–1441 (2008).
[13] Ouedraogo, E., Lasaygues, P., Lefebvre, J., Talmant, M., Gindre, M.., Laugier, P., "Multi-step compensation technique for ultrasound tomography of bone," Acoust. Imaging **26**, 153–160 (2002).
[14] Treeby, B. E., Jaros, J., Rendell, A. P.., Cox, B. T., "Modeling nonlinear ultrasound propagation in heterogeneous media with power law absorption using a k-space pseudospectral method.," J. Acoust. Soc. Am. **131**(6), 4324–4336 (2012).
[15] Goss, S. A., Johnston, R. L.., Dunn, F., "Comprehensive compilation of empirical ultrasonic properties of mammalian tissues.," J. Acoust. Soc. Am. **64**(2), 423–457 (1978).
[16] Goss, S. A., Johnston, R. L.., Dunn, F., "Compilation of empirical ultrasonic properties of mammalian tissues. II," J. Acoust. Soc. Am. **68**(1), 93–108 (1980).
[17] Li, C., Huang, L., Duric, N., Zhang, H.., Rowe, C., "An improved automatic time-of-flight picker for medical ultrasound tomography," Ultrasonics **49**(1), 61–72 (2009).
[18] Norton, S. J., "Reconstruction of a two-dimensional reflecting medium over a circular do main: Exact solution," J. Acoust. Soc. Am. **67**(4), 1266 (1980).
[19] Baysal, E., Kosloff, D. D.., Sherwood, W. C., "Reverse time migration," Geophysics **48**(11), 1514–1524 (1983).
[20] Jones, I. F., "Tutorial: Migration imaging conditions," First Break **32**(12), 45–55 (2014).
[21] Qin, F., Luo, Y., Olsen, K. B., Cai, W.., Schuster, G. T., "Finite-difference solution of the eikonal equation along expanding wavefronts," Geophysics **57**(3), 478 (1992).
[22] Vidale, J., "Finite-Dofference calculation of travel times," Bull. Seismol. Soc. Am. **78**(6), 2062–2076 (1988).
[23] Bar, L., Kiryati, N.., Sochen, N., "Image deblurring in the presence of impulsive noise," Int. J. Comput. Vis. **70**(3), 279–298 (2006).